SCIENTIFIC REPORTS

OPEN

The thermal and electrical properties of the promising semiconductor MXene Hf_2CO_2

Received: 15 December 2015
Accepted: 27 May 2016
Published: 15 June 2016

Xian-Hu Zha[1], Qing Huang[1], Jian He[2], Heming He[3], Junyi Zhai[4], Joseph S. Francisco[5] & Shiyu Du[1]

With the growing interest in low dimensional materials, MXenes have also attracted considerable attention recently. In this work, the thermal and electrical properties of oxygen-functionalized M_2CO_2 (M = Ti, Zr, Hf) MXenes are investigated using first-principles calculations. Hf_2CO_2 is determined to exhibit a thermal conductivity better than MoS_2 and phosphorene. The room-temperature thermal conductivity along the armchair direction is determined to be 86.25~131.2 $Wm^{-1}K^{-1}$ with a flake length of 5~100 μm. The room temperature thermal expansion coefficient of Hf_2CO_2 is 6.094×10^{-6} K^{-1}, which is lower than that of most metals. Moreover, Hf_2CO_2 is determined to be a semiconductor with a band gap of 1.657 eV and to have high and anisotropic carrier mobility. At room temperature, the Hf_2CO_2 hole mobility in the armchair direction (in the zigzag direction) is determined to be as high as 13.5×10^3 $cm^2V^{-1}s^{-1}$ (17.6×10^3 $cm^2V^{-1}s^{-1}$). Thus, broader utilization of Hf_2CO_2, such as the material for nanoelectronics, is likely. The corresponding thermal and electrical properties of Ti_2CO_2 and Zr_2CO_2 are also provided. Notably, Ti_2CO_2 presents relatively lower thermal conductivity but much higher carrier mobility than Hf_2CO_2. According to the present results, the design and application of MXene based devices are expected to be promising.

Because two-dimensional (2D) materials exhibit many novel electronic and thermal properties that differ from those of their bulk counterparts, these materials have received considerable attention over the past two decades. For example, the adoption of 2D materials in place of traditional bulk materials for the next generation of electronic devices has recently been demonstrated as a potentially practical strategy[1]. Since the size of electronic devices has been continuously decreasing over the past twenty years during the development of highly integrated electronic components, efficient heat dissipation, a moderate electronic band gap and a reasonably high carrier mobility[2] have become equally important properties in determining the performance of electronic devices. Graphene, a well-known 2D carbon material[3], has been demonstrated to possess a high thermal conductivity and high charge carrier mobility[4], which have strongly encouraged ongoing research into expanding its applicability as a material for thermal conduction or electronic devices. Many other similar classes of 2D materials have also been fabricated as candidate materials for nanoelectronics, including monolayers of h-BN[5], phosphorene[2,6–8], and transition-metal dichalcogenides[9,10]. In-depth investigations of these monolayers have been conducted and have led to several potential applications[11]. However, additional treatment on these 2D materials is generally required, such as structural modification, composition, or application of external fields[11] for their practical application in highly integrated electronic components. The reasons for these requirements are as follows: graphene is a zero-band-gap semiconductor in nature and thus its band gap needs to be opened[12]; monolayer h-BN[13] has an excessively large band gap (5.5 eV); the thermal conductivities of monolayer MoS_2 and phosphorene [(34.5 ± 4) and 11.8 $Wm^{-1}K^{-1}$, respectively] are not impressive in terms of heat dissipation[7,14]. Moreover, the carrier mobility of MoS_2 is not ideally high[15], and phosphorene is prone to chemical degradation upon exposure to ambient conditions[16]. In other words, difficulties may occur if these materials are directly applied in highly integrated electronic

[1]Engineering Laboratory of Specialty Fibers and Nuclear Energy Materials, Ningbo Institute of Materials Technology and Engineering, Chinese Academy of Sciences, Ningbo, Zhejiang, 315201, China. [2]Center for Translational Medicine, Department of Biotechnology, Dalian Institute of Chemical Physics, Chinese Academy of Sciences, Dalian, Liaoning, 116023, China. [3]State Nuclear Power Research Institute, Beijing, 100029, China. [4]Beijing Institute of Nanoenergy and Nanosystems, Chinese Academy of Sciences, Beijing 10083, China. [5]Departments of Chemistry and Earth and Atmospheric Science, Purdue University, West Lafayette, IN 47906, USA. Correspondence and requests for materials should be addressed to S.D. (email: dushiyu@nimte.ac.cn)

components considering their intrinsic properties. Therefore, the discovery of a desirable 2D semiconducting material with a moderate band gap, satisfactory intrinsic thermal conductivity and high carrier mobility remains a primary goal of research in physics and materials science.

Recently, a new family of 2D transition-metal carbides and nitrides called "MXene"[17–22] has been fabricated by selective etching of "A" from $M_{n+1}AX_n$ phases (where M is an early transition metal, A is an A-group element, X is C and/or N, and n = 1, 2, or 3). Since $M_{n+1}AX_n$ materials represent a large family that consists of more than 60 members[23], the corresponding MXenes inherit versatile configurations. To date, the following MXenes have been synthesized by exfoliation of the corresponding $M_{n+1}AX_n$ phases and relatives with a hydrofluoric acid treatment: Ti_3C_2[17], Ti_2C, Ta_4C_3, TiNbC, $(V_{0.5}, Cr_{0.5})_3C_2$, Ti_3CN[18], Z_3C_2[24], Mo_2TiC_2, $Mo_2Ti_2C_3$, Cr_2TiC_2[25], Nb_4C_3[22], Mo_2C[26], Nb_2C and V_2C[19]. The as-synthesized MXenes are typically functionalized by -O, -OH and -F groups. Naguib *et al.*[21] have published a review of these materials in which they denote functionalized MXenes as $M_{n+1}X_nT_x$, with T standing for the surface-terminating group. Both theoretical and experimental results have demonstrated that MXenes have potential applications in hydrogen storage[27], lithium-ion batteries (LIBs)[28,29], supercapacitors[30,31], adsorbents[32,33] and electronic devices[34,35]. As the attention on this new class of MXene materials grows, gaining deeper insight into their basic physical properties becomes more important. However, only few studies[36,37] have been published in the literature on the thermal properties and carrier mobility of MXene materials.

In this work, the electronic band gap, thermal properties and carrier mobility of three oxygen-functionalized MXenes, Ti_2CO_2, Zr_2CO_2 and Hf_2CO_2, are predicted via theoretical calculations. Oxygen-functionalized MXenes are chosen in this work for their current applicability compared to those functionalized by -F and -OH groups[29,38–41] and for their higher thermodynamic stability[38]. Based on the results presented herein, Hf_2CO_2 is unexpectedly determined to possess a moderate band gap, a thermal conductivity better than MoS_2 and phosphorene, and a high carrier mobility comparable to phosphorene, which indicates that this material may have extensive potential applications in nanoelectronics. For this reason, the major part of this work focuses on the thermal conductivity and electrical properties of Hf_2CO_2. In addition, the specific heat and thermal expansion coefficient of Hf_2CO_2 are provided as well. The corresponding values for Ti_2CO_2 and Zr_2CO_2 are also examined and discussed for comparison to the results for Hf_2CO_2. According to the computational results, the thermal conductivity increases with increasing atomic number of M among M_2CO_2 (M = Ti, Zr, Hf) MXenes and all the three MXenes present high carrier mobilities. Moreover, Ti_2CO_2 are found to possess much lower thermal conductivity and higher hole mobility than Zr_2CO_2 and Hf_2CO_2. The results for Ti_2CO_2 and Zr_2CO_2 are mainly supplied in the Supplementary Information.

Results

The geometries and electronic properties of Hf_2CO_2 are investigated using DFT calculations. The Hf_2CO_2 MXene shows a hexagonal lattice with its space group of $P\bar{3}M1$(No. 164). Similar to graphene and other 2D hexagonal materials[11], the MXene possesses two high-symmetry routes namely the armchair and zigzag directions. Seen from the top-view as shown in Fig. 1a, the x-axis coincides with the zigzag direction, and the y-axis is parallel to the armchair direction in our model. Moreover, based on the hexagonal lattice, the ΓM route in the Brillouin zone (BZ) corresponds to the armchair direction in the real-space, and the ΓK vector is along the zigzag direction as presented in Fig. 1b. The periodicities along the two high symmetry directions can be more clearly displayed with an orthorhombic lattice as shown in Fig. 1c. Evidently, the basis vector along the zigzag direction is smaller than that in the armchair direction, whose length is determined to be $\sqrt{3}/3$ of that for the latter. As seen from the side-view in Fig. 1d, a central carbon monolayer is sandwiched between two Hf layers, and the oxygen layer is directly projected to the bottom Hf layer on both sides. The stable structure is similar to those of other stable oxygen-functionalized M_2CO_2 (M is a transition metal) MXenes[42], including Ti_2CO_2 and Zr_2CO_2, whose geometries differ only slightly from Hf_2CO_2 in bond lengths and lattice constants. To be more explicitly, the lattice parameters, layer thicknesses, bond lengths and atomic charges for these three MXenes are given in Table 1. Evidently, the Zr_2CO_2 shows the largest atomic charges, and the atomic charges in Ti_2CO_2 are significantly smaller, which reflects that Zr_2CO_2 possesses stronger bonds than Ti_2CO_2. The lattice parameter and unit cell volume of Hf_2CO_2 appear to be smaller than Zr_2CO_2 despite that Hf has a larger atomic radius than Zr, showing the strength of the bonds may be stronger in Hf_2CO_2 compared to that in Zr_2CO_2. Therefore, the mechanical strength increases with the increasing atomic number of M among these three MXenes[41]. Figure 1e depicts the electronic energy band of Hf_2CO_2. From GGA calculations, Hf_2CO_2 is an indirect semiconductor with a band gap of 1.021 eV, which agrees well with previous findings[42]. After HSE06 correction, this band gap increases to 1.657 eV, which is comparable to those of monolayer MoS_2 and phosphorene[2,9]. Since the HSE method is demonstrated to yield a 0.3 eV mean absolute error smaller than semiconductors' band gaps[43], the true band gap for Hf_2CO_2 may reach 1.957 eV. Figure 1f shows the electronic energy band based on the orthorhombic lattice, in which the conduction-band minimum (CBM) is folded to the Γ point. Two sub-bands overlap at the valance-band maximum (VBM), with an energy difference of only 0.6 meV at the Γ point (the corresponding difference at the Γ point is 1.8 meV in the case of Ti_2CO_2, and 0.3 meV for Zr_2CO_2). All of the M_2CO_2 (M = Sc, Ti, Zr, Hf, V, Nb, Ta, Cr, Mo, W) electronic band structures based on GGA calculations are provided in Fig. S1. The M_2CO_2 (M = Sc, Ti, Zr, Hf, W) MXenes are found to be semiconductors, which is consistent with our previous work[41]; their electronic energy bands are corrected by HSE06 functional. Due to its semiconducting behavior, the electronic thermal conductivity in Hf_2CO_2 is negligible.

The Hf_2CO_2 phonon dispersions along the armchair (ΓM) and zigzag (ΓK) directions are shown in Fig. 2a,b, respectively. The out-of-plane acoustic (ZA), longitudinal acoustic (LA) and transversal acoustic (TA) modes are denoted with black squares, red circles and blue triangles, respectively. The ZA mode nearly coincides with the TA mode in the armchair direction, differing from that along the zigzag direction. From the phonon dispersion, the group velocities of the acoustic modes in the armchair direction are determined as $\nu_{ZA} = 1.826 \times 10^3\,ms^{-1}$, $\nu_{TA} = 1.919 \times 10^3\,ms^{-1}$ and $\nu_{LA} = 2.065 \times 10^3\,ms^{-1}$, and the corresponding group velocities in the zigzag direction

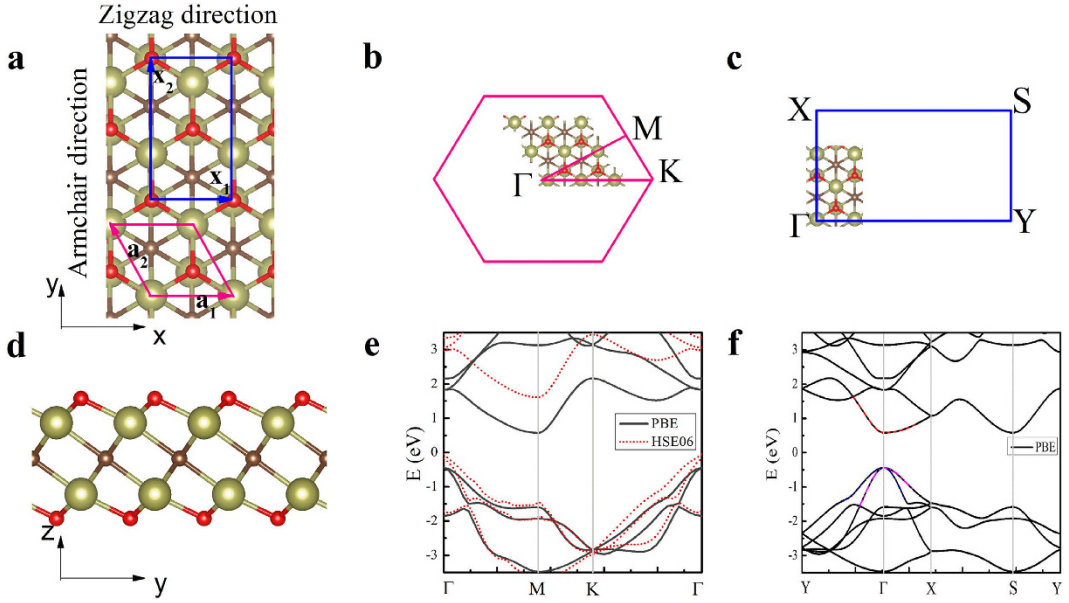

Figure 1. Structure and electronic band structure of Hf_2CO_2. (**a**) Top-view of the Hf_2CO_2 structure; the hexagonal unit cell and orthorhombic cell are circled in pink and blue boxes, respectively; the *x*- (*y*-) axis corresponds to the Hf_2CO_2 zigzag (armchair) direction. (**b**) The Brillouin zone (BZ) of the hexagonal unit cell; the ΓM (ΓK) direction in reciprocal space corresponds to the Hf_2CO_2 armchair (zigzag) direction in real space. (**c**) The BZ of the Hf_2CO_2 orthorhombic cell. (**d**) The side-view of Hf_2CO_2. (**e**) The electronic band structure of Hf_2CO_2. The band gap is increased using the HSE06 correction. The Fermi level is located at 0 eV. (**f**) The Hf_2CO_2 electronic band structure based on the orthorhombic cell. The valance band maximum (VBM) and conduction band minimum (CBM) are denoted by colored lines.

MXenes	a (Å)	*h* (Å)	Bond length (Å)		Atomic charge		
			M-C	M-O	M	C	O
Ti_2CO_2	3.036	6.883	2.187	1.978	1.732	−1.497	−0.981
Zr_2CO_2	3.310	6.191	2.368	2.120	2.238	−1.954	−1.258
Hf_2CO_2	3.266	6.029	2.333	2.103	2.079	−1.848	−1.151

Table 1. The lattice parameters, layer thicknesses, bond lengths and atomic charges for M_2CO_2 (M = Ti, Zr, Hf) MXenes.

are $\nu_{ZA} = 1.641 \times 10^3\,ms^{-1}$, $\nu_{TA} = 2.075 \times 10^3\,ms^{-1}$ and $\nu_{LA} = 1.656 \times 10^3\,ms^{-1}$. The value of Grüneisen parameter γ_j representing MXene anharmonic effect is determined from the phonon dispersions using optimized ($a = 1.00\,a_0$ where a_0 is the optimized hexagonal lattice parameter in the plane parallel to BZ) and strained ($a = 0.99a_0$ and $a = 1.01a_0$) configurations. From the calculations with the conventional method[44], γ_j for the acoustic modes of Hf_2CO_2 are $\gamma_{ZA} = -0.164$, $\gamma_{TA} = -1.254$ and $\gamma_{LA} = 1.032$ in the armchair direction and $\gamma_{ZA} = -0.263$, $\gamma_{TA} = -0.916$ and $\gamma_{LA} = 1.240$ in the zigzag direction. Evidently, the group velocities are larger and Grüneisen parameters are smaller for the ZA and LA modes in the armchair direction than those in the zigzag direction, and the TA mode shows the opposite trend. The values of $<\gamma_j^2>$ as well as γ_j and υ_j used for calculating the thermal conductivities of M_2CO_2 (M = Ti, Zr, Hf) MXenes are given in Table 2. Generally, υ_j and γ_j decrease with the increasing atomic number of M among M_2CO_2 (M = Ti, Zr, Hf) MXenes. The Hf_2CO_2 thermal conductivities along the armchair and zigzag directions are calculated using Equation (1); the results are depicted in Fig. 2c,d, respectively. A flake length of 5 μm is adopted in both cases. According to the figures, the Hf_2CO_2 thermal conductivity is strongly anisotropic due to the anisotropic group velocities and Grüneisen parameters as indicated above. This can be qualitatively understood from the atomic arrangement of Hf_2CO_2. As seen in Fig. 1a, the projections of some Hf-O and Hf-C bonds on the material plane are parallel to the armchair direction, whereas no projections of any bonds can coincide with the zigzag direction, which causes different interatomic force in vibration propagating along different directions. Consequently, the phonon frequencies and group velocities are different between the sound waves propagating along the armchair and zigzag directions. Moreover, the different bonding strengths projected to the two directions also causes different anharmonic effects, leading to anisotropic Grüneisen parameters. Therefore, the anisotropy of the thermal conductivity can essentially be attributed to the atomic configuration of the MXene. In the armchair direction, the room temperature thermal conductivity is determined to be 86.25 $Wm^{-1}K^{-1}$, the corresponding value in the zigzag direction is only 42.3% of the former. In both directions, the thermal conductivity is mainly contributed by ZA and LA modes, with the contribution from ZA mode is slightly higher. For

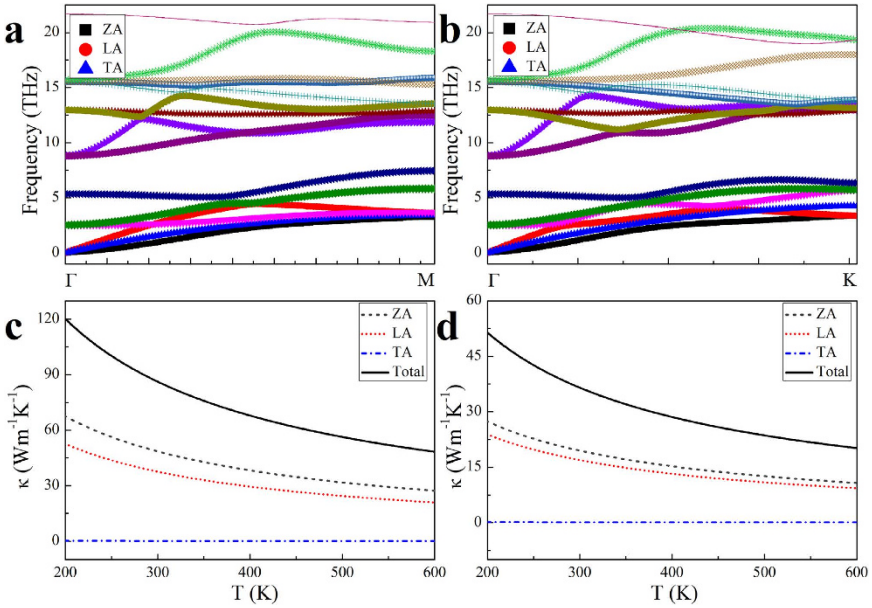

Figure 2. Phonon dispersions and thermal conductivities along the armchair (ΓM) and zigzag (ΓK) directions. (**a**) The phonon dispersion of Hf_2CO_2 along the armchair direction. The out-of-plane acoustic (ZA), longitudinal acoustic (LA) and transversal acoustic (TA) modes are denoted with black squares, red circles and blue triangles, respectively. (**b**) The phonon dispersion of Hf_2CO_2 along the zigzag direction. (**c**) The temperature dependence of the Hf_2CO_2 thermal conductivity along the armchair direction. The ZA, LA and LA mode contributions to the thermal conductivity are denoted with grey dashed, red dotted and blue dash-dotted lines, respectively. (**d**) The temperature dependence of the Hf_2CO_2 thermal conductivity along the zigzag direction.

MXenes		υ_j (10^3 ms^{-1})			γ_j			$<\gamma_j^2>$		
		ZA	TA	LA	ZA	TA	LA	ZA	TA	LA
Ti_2CO_2	Armchair	2.566	2.666	2.974	−5.348	4.374	1.737	4088	20.42	5.379
	Zigzag	2.252	2.974	2.279	−4.457	4.317	2.252	4089	19.83	6.705
Zr_2CO_2	Armchair	2.379	2.518	2.715	−0.573	2.432	1.231	19.79	6.155	2.639
	Zigzag	2.113	2.640	2.136	−2.008	3.039	1.433	298.1	10.13	2.911
Hf_2CO_2	Armchair	1.826	1.919	2.066	−0.164	−1.254	1.032	1.256	1382	2.088
	Zigzag	1.641	2.075	1.656	−0.263	−0.916	1.240	2.316	1392	2.391

Table 2. Parameters for calculating the thermal conductivities of M_2CO_2 (M = Ti, Zr, Hf) MXenes.

example, in the armchair direction, the ZA and LA modes' contributions to the thermal conductivity at room temperature are 48.55 and 37.58 $Wm^{-1}K^{-1}$, respectively. However, the large contribution of ZA mode to thermal conductivity is absent in Ti_2CO_2 and Zr_2CO_2, as shown in Figs S2 and S3, respectively. For these two M_2CO_2 (M = Ti, Zr) MXenes, their conductivities are mainly contributed by TA and LA modes.

For comparison, we plot the thermal conductivities of all the three M_2CO_2 (M = Ti, Zr, Hf) MXenes in Fig. 3 based on a 5 μm flake length. Figure 3a shows the thermal conductivities in the armchair direction, and Fig. 3b depicts those in the zigzag direction. Evidently, all the three MXenes present strong anisotropic thermal conductivities, and the ratios between the zigzag and armchair thermal conductivities of M_2CO_2 (M = Ti, Zr, Hf) MXenes are 54.4%, 46.2% and 42.3% respectively. One can also find that the thermal conductivity increases significantly with increasing atomic number of M in both directions. As an example, the room temperature thermal conductivities of Ti_2CO_2 in armchair direction is determined to be 21.88 $Wm^{-1}K^{-1}$, while the corresponding values in Zr_2CO_2 and Hf_2CO_2 increase to 61.93 and 86.25 $Wm^{-1}K^{-1}$, respectively. As to the zigzag direction, the room temperature values for M_2CO_2 (M = Ti, Zr, Hf) MXenes follows the similar trend, which are 11.91, 28.59, 36.51 $Wm^{-1}K^{-1}$ respectively. This can be explained by the enhanced mechanical strengths of MXenes with increasing atomic number of M[41]. The thermal conductivity of Hf_2CO_2 in armchair direction is higher than those of many well-known thermal conductive materials, such as pure iron[45], suggesting that Hf_2CO_2 may have satisfactory performance in heat conduction as a 2D oxide material. Additionally, it is worthy of accentuating that the thermal conductivity of Hf_2CO_2 is higher than those of MoS_2 and phosphorene which are well known promising semiconducting 2D materials for nanoelectronics.

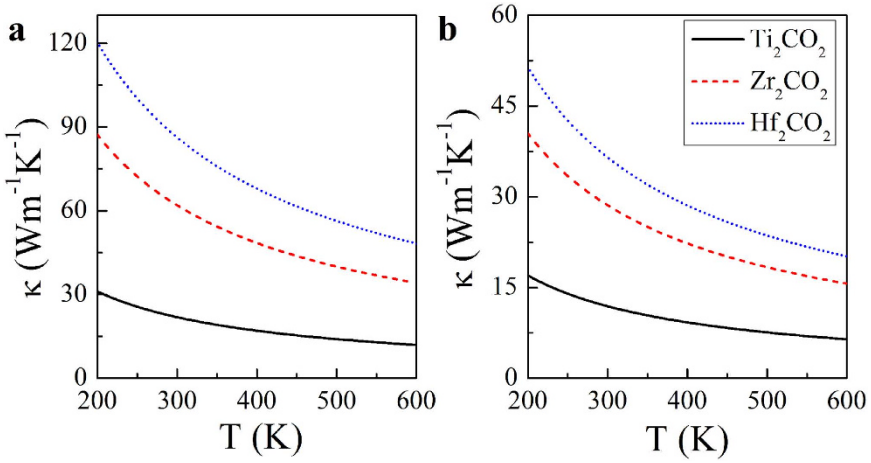

Figure 3. The temperature dependence of the thermal conductivities of the M_2CO_2 (M = Ti, Zr, Hf) MXenes. (**a**) The temperature dependence of the thermal conductivities of the M_2CO_2 (M = Ti, Zr, Hf) MXenes along the armchair direction. The Ti_2CO_2, Zr_2CO_2 and Hf_2CO_2 thermal conductivities are denoted in black solid, red dashed and blue dotted lines, respectively. (**b**) The temperature dependence of the thermal conductivities of the M_2CO_2 (M = Ti, Zr, Hf) MXenes along the zigzag direction.

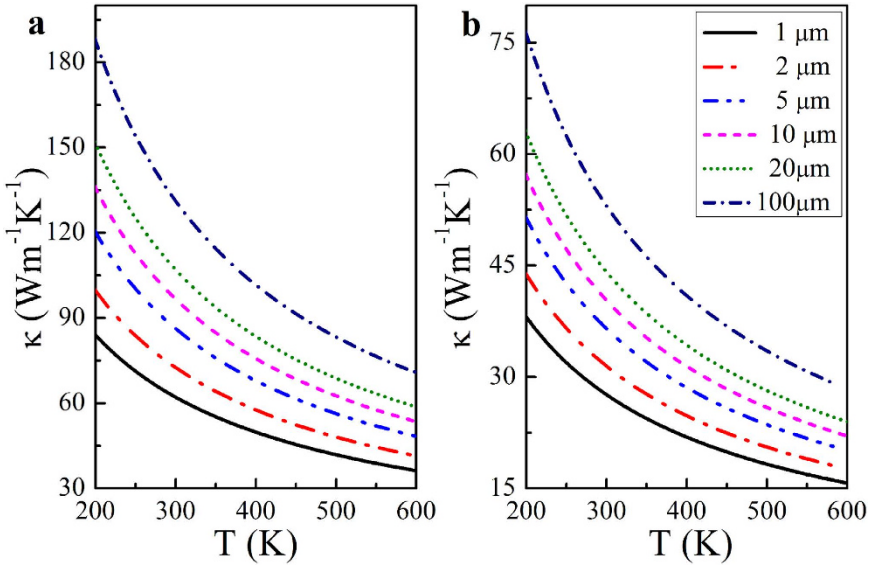

Figure 4. The temperature dependence of Hf_2CO_2 thermal conductivity with varying flake lengths. (**a**) The temperature dependence of the thermal conductivity with varying flake lengths in the armchair direction. The thermal conductivity for flake lengths of 1, 2, 5, 10, 20 and 100 μm are denoted by black solid, red dash-dotted, blue dashed-dotted, magenta dashed, olive dotted and navy dash-dotted lines, respectively. (**b**) The temperature dependence of the Hf_2CO_2 thermal conductivity with varying flake lengths in the zigzag direction.

Because of boundary scattering, the thermal conductivity is dependent upon the flake length*d*. The theoretical thermal conductivity of Hf_2CO_2 with flake lengths from 1 to 100 μm in the armchair and zigzag directions are shown in Fig. 4a,b, respectively. The thermal conductivity increases monotonically with increasing flake length in both directions. Moreover, the thermal conductivity is more sensitive to the flake length at low temperatures. At room temperature, the thermal conductivity in the zigzag direction increases from 27.63 to 53.03 $Wm^{-1}K^{-1}$, for a flake-length increase from 1 to 100 μm. With the same range of the flake length, the room temperature thermal conductivity in the armchair direction ranges from 62.12 to 131.2 $Wm^{-1}K^{-1}$. These results further confirm the capability of Hf_2CO_2 for heat dissipation if used in an electronic device.

The specific heat and thermal expansion coefficient are also studied from the phonon dispersion for the hexagonal BZ of Hf_2CO_2 (Fig. 5a). The specific heat and thermal expansion coefficient are presented in Fig. 5b,c, respectively. The results show that the specific heat and thermal expansion coefficient increase with increasing temperature and that the room-temperature values are 0.238×10^3 $Jkg^{-1}K^{-1}$ and 6.094×10^{-6} K^{-1}, respectively. The room-temperature thermal expansion coefficient is lower than that for most metals, such as 16.50×10^{-6} K^{-1}

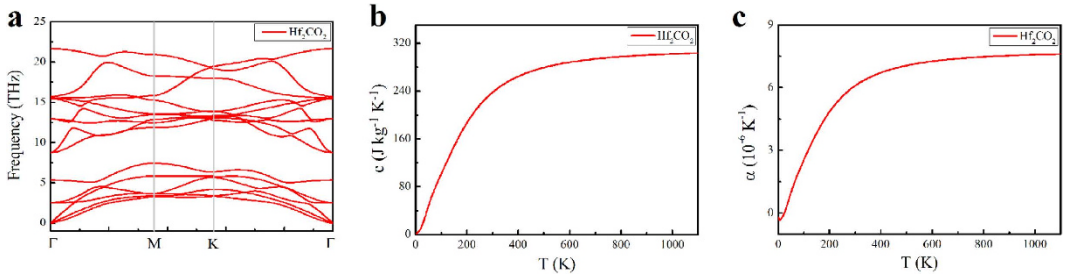

Figure 5. The phonon dispersion, specific heat and thermal expansion coefficient of Hf_2CO_2. (**a**) The phonon dispersion of Hf_2CO_2 in the BZ. (**b**) The temperature dependence of Hf_2CO_2 specific heat. (**c**) The temperature dependence of the Hf_2CO_2 thermal expansion coefficient.

Carrier type	m_{ex}^*/m_0	m_{ey}^*/m_0	$E1x$ (eV)	$E1y$ (eV)	Cx (Jm^{-2})	Cy (Jm^{-2})	μx ($10^3\,cm^2V^{-1}s^{-1}$)	μy ($10^3\,cm^2V^{-1}s^{-1}$)
e	0.231	2.162	10.57	7.101	293.6	291.0	0.329	0.077
h (upper)	0.423	0.164	7.636	2.297	293.6	291.0	0.924	26.0
h (lower)	0.164	0.414	2.023	7.422	293.6	291.0	34.3	1.00

Table 3. Hf_2CO_2 carrier mobility. Carrier types "e" and "h" denote "electron" and "hole," respectively. m_{ex}^* and m_{ey}^* are the effective masses along the zigzag (x-) and armchair (y-) directions, respectively. E_{1x} and E_{1y} are the deformation potential constants, and C_x and C_y are the elastic moduli. μ_x and μ_y are the room-temperature carrier mobilities.

for bulk copper. The low thermal expansion coefficient is another advantage of Hf_2CO_2 in applications requiring structural stability at varying temperatures such as in electronic devices.

In the calculation of carrier mobility, the orthorhombic cell is adopted, which makes the elastic modulus along the transport direction well defined. Moreover, it facilitates the determination of the electron effective masses in the x- and y-directions. Before predicting the carrier mobility of Hf_2CO_2, we perform a benchmark calculation on the electron mobility of phosphorene. The room-temperature electron mobility of phosphorene is determined to be 1.387×10^3 and $0.177 \times 10^3\,cm^2V^{-1}s^{-1}$ along the armchair and zigzag directions, respectively, which is in good agreement with the results of previous works[2,8]. In this study, both the electron and hole mobilities of Hf_2CO_2 are evaluated and the results are listed in Table 3. The electron mobilities are found highly anisotropic, and the values along the zigzag (x-) and armchair (y-) directions are 0.329×10^3 and $0.077 \times 10^3\,cm^2V^{-1}s^{-1}$, respectively, at room temperature. As to the calculations for hole mobilities, one should notice that two quasi-degenerated sub-bands appear at the VBM as shown in Fig. 1f. Hence, the hole mobilities of both sub-bands should be calculated and the total hole mobility can be estimated as the statistical average of the two sub-bands on the basis of Boltzmann's distribution. For clear elaboration, we denote the sub-band with a higher (lower) energy at the Γ point as the "upper" ("lower") band in Table 3. From the "upper" sub-band (denoted in blue in Fig. 1f), the hole mobilities are determined to be 0.924×10^3 and $26.0 \times 10^3\,cm^2V^{-1}s^{-1}$ along the Hf_2CO_2 zigzag and armchair directions, respectively. Correspondingly, the hole mobilities of the "lower" band (denoted in megaton in Fig. 1f) are calculated as 34.3×10^3 and $1.00 \times 10^3\,cm^2V^{-1}s^{-1}$ along the zigzag and armchair directions of Hf_2CO_2, respectively. The high hole mobilities are mainly caused by the small hole effective mass and low deformation potential constant, as described in the table. Notably, the effective masses and deformation potential constants for the two sub-bands are close to each other in value, but their directions appear to be opposite. For the "upper" sub-band, the hole effective mass and deformation potential constant in the zigzag direction are both approximately three-fold higher than those in the armchair direction, causing the highly anisotropic hole mobility (approximately twenty-eight-fold higher in the armchair direction). However, the sequence of hole mobilities along the two directions for the "lower" sub-band are totally reversed reflected by the seemingly "exchanged" effective masses and deformation potential constants. Consequently, the average hole mobilities exhibit only slight anisotropy, which are 17.6×10^3 and $13.5 \times 10^3\,cm^2V^{-1}s^{-1}$ along the Hf_2CO_2 zigzag and armchair directions, respectively. Evidently, the predicted hole mobility is much higher than the electron mobility, which can be ascribed to the lighter effective masses and smaller deformation potential constants of the holes as presented in Table 3. The predicted high carrier mobilities are much higher than that of monolayer MoS_2[15], and they are comparable to the hole mobility of monolayer phosphorene[2] along the zigzag direction. Moreover, the oxygen functionalized Hf_2CO_2 MXene may show higher stability than phosphorene. Thus, the current results indicate that Hf_2CO_2 may perform well as a material in nanoelectronics.

Different from the anisotropy of the phonon thermal conductivity caused by the MXene atomic configurations, the carrier mobility is mainly related to the electronic wavefunctions at the VBM and CBM. Therefore, to understand the difference in anisotropy between the electron and hole mobilities, the electronic wavefunctions for the CBM and VBM (the sum of "upper" and "lower" sub-bands) on the basis of the orthorhombic cell are plotted in Fig. 6. From the figure, the electronic wavefunctions of CBM are mainly contributed by the hafnium and oxygen atoms, and the wavefunctions show clear delocalization feature along the zigzag direction but there exist

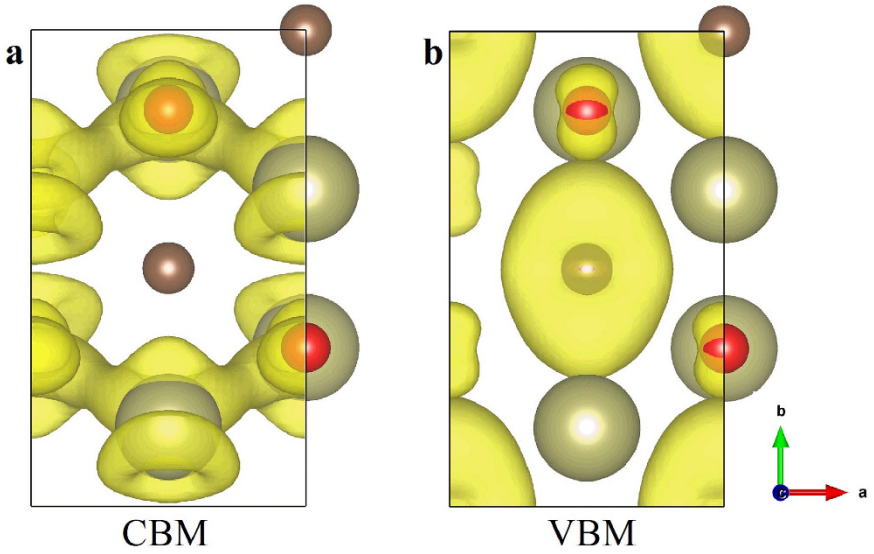

Figure 6. The electronic wavefunctions of the CBM and VBM for Hf_2CO_2 based on the orthorhombic cell. (**a**) CBM. (**b**) VBM.

nodes along the armchair direction. Thus, the electron mobility is much larger in the zigzag direction. Regarding to the electronic wavefunctions for the VBM as shown in Fig. 6b, they are mainly from the carbon atoms and nodes can be found along both directions, which is different from the CBM. Accordingly, the hole mobility of the Hf_2CO_2 present only slight anisotropy.

The carrier mobilities of Ti_2CO_2 and Zr_2CO_2 are also calculated, as shown in Tables S1 and S2, respectively. It is noteworthy that Ti_2CO_2 presents much higher hole mobility compared with Zr_2CO_2 and Hf_2CO_2. The statistical average hole mobility of Ti_2CO_2 is predicted to be 33.6×10^3 and $26.6 \times 10^3\,cm^2V^{-1}s^{-1}$ along the zigzag and armchair directions, respectively, which are approximately two fold greater than that of Hf_2CO_2. The predicted high hole mobilities are well consistent with the experimental findings for Ti_2CT_x MXene[37], in which the room temperature carrier mobility is measured to be in order of $10^4\,cm^2V^{-1}s^{-1}$. The consistency between our work and experimental measurement further indicates the reliability of our calculations. In addition, Khazaei *et al.* have demonstrated Ti_2CO_2 possesses a large Seebeck coefficient [46]. This implies that Ti_2CO_2 may be applicable as thermoelectric materials[47] because of the low thermal conductivity and high carrier mobility determined here. Furthermore, Ti_2CO_2 may be preferred over Hf_2CO_2 for use in electronic devices in cases heat dissipation is not the major concern.

Discussion

The combination of the results for the carrier mobilities with those for the thermal properties suggests that Hf_2CO_2 is a good choice for nanoelectronics applications. Because of the limited data currently available, further research should be conducted on the synthesis of M_2CO_2 (M = Zr, Hf) monolayers, and their intrinsic thermal and electrical properties should be experimentally measured. Considering the successful fabrication of Ti_2CT_2 (T = -O, -F, -OH) and the existence of MAX phases M_2AC (M = Zr, Hf; A = In, Tl, Sn, Pb, S)[48], there is a great anticipation on the synthesis of M_2CO_2 (M = Zr, Hf) using the reported preparation methods such as etching of their parental MAX phase and heat treatment on hydroxyl functionalized MXenes. We look forward to more findings reported for these three MXenes from the forthcoming experimental studies.

In summary, the thermal and electrical properties of Hf_2CO_2 are investigated. The Hf_2CO_2 band gap is determined to be 1.657 eV. The thermal conductivity of Hf_2CO_2 in the armchair direction at room temperature is predicted to be $86.25\,Wm^{-1}K^{-1}$ with a flake length of $5\,\mu m$; this thermal conductivity is higher than those of pure iron and some other well known two dimensional materials including MoS_2 and phosphorene. Moreover, the Hf_2CO_2 thermal conductivity is anisotropic with the thermal conductivity in the zigzag direction only 42.3% of that in the armchair direction at room temperature. In addition, the thermal expansion coefficient of Hf_2CO_2 is lower than that of most metals. The carrier mobility of Hf_2CO_2 is also predicted, with consideration of electron-phonon coupling. The room-temperature hole mobility in the armchair (zigzag) direction is calculated to be as high as $13.5 \times 10^3\,cm^2V^{-1}s^{-1}$ ($17.6 \times 10^3\,cm^2V^{-1}s^{-1}$). Therefore, Hf_2CO_2 can be considered as candidate 2D materials for the design of next-generation electronic devices. The carrier mobility of Ti_2CO_2 is determined to be two fold higher than that of Hf_2CO_2 while the thermal conductivity is much lower. According to the current results, Ti_2CO_2 can be considered as candidate 2D thermoelectric materials and it may also be a better option than Hf_2CO_2 for nanoelectronics if good heat dissipation can be achieved in a device. Finally, options for further explorations of MXenes are raised on the basis of the results from the present work.

Methods

The calculated structures and electronic properties are determined on the basis of first-principles density functional theory implemented in the plane-wave VASP code[49]. The generalized gradient approximation (GGA) of the Perdue-Burke-Ernzerhof (PBE)[50] scheme is adopted for the exchange-correlation functional. To obtain a more reliable band gap, the Heyd-Scuseria-Ernzerhof (HSE06)[51,52] hybrid functional is utilized to calculate the electronic energy bands of M_2CO_2 (M = Ti, Zr, Hf) hexagonal unit cells. The projected augmented wave (PAW) approach[53] is employed for pseudopotentials; the plane-wave cutoff energy is chosen to be 500 eV. The conjugate gradient[54] method is applied for structural optimization, and the system is relaxed until the forces on each atom are less than 1.0×10^{-4} eV/atom. To eliminate neighboring layer interaction, a 25-Å vacuum layer parallel to the surface layer is used. During optimization, a $12 \times 12 \times 1$ k-points mesh is sampled in the Brillouin zone (BZ), and a 60 k-points grid is applied for plotting the electronic energy band. To investigate the atomic charge of each atom in the investigated MXenes, the Bader charge analysis[55] based on a $180 \times 180 \times 1$ mesh is adopted. All of the structures are visualized using the VESTA code[56].

The thermal properties, including the phonon thermal conductivity, specific heat, and thermal expansion coefficient, are calculated from the phonon dispersion of a hexagonal unit cell, as circled in the pink rhombus in Fig. 1a. A 120 k-points grid is employed for plotting the phonon dispersion for various directions and the entire BZ. The Phonopy software[57] combined with the VASP code is utilized for phonon dispersion calculations. The theoretical calculation is performed with the density functional perturbation theory (DFPT)[58], and a $6 \times 6 \times 1$ k-points mesh based on a $4 \times 4 \times 1$ supercell is adopted for calculating the dynamical matrix. The phonon band connections are estimated from eigenvectors and the phonon band is determined considering band crossings implemented in the Phonopy software. The phonon thermal conductivity is calculated within the framework of Klemens' theory[59,60]:

$$\kappa_{ph} = \sum_j \frac{\rho}{<\gamma_j^2>} \frac{<\upsilon_j>^4}{\omega_{\max,j} T} \ln \frac{\omega_{\max,j}}{\omega_{\min,j}} \quad (1),$$

where T is temperature, $\omega_{\max,j}$ and $\omega_{\min,j}$ are the maximum and minimum circular frequency of each j^{th} branch. υ_j represents the group velocity along the temperature gradient. Due to the finite flake length L, the term of $\omega_{\min,j}$ is redefined as: $\omega_{\min,j} = \left(\frac{M < \upsilon_j >^3 \omega_{\max,j}}{2 < \gamma_j^2 > k_B T L} \right)^{\frac{1}{2}}$[60], with M being the mass of the MXene unit cell. k_B is the Boltzmann constant. γ_j is the average value of the j^{th} branch Grüneisen parameter, and $<\gamma_j^2>$ in Equation (1) is estimated by $<\gamma_j^2> = \frac{\sum_k \gamma_{j,k}^2 C_{j,k}}{\sum_k C_{j,k}}$[59]. Variable ρ represents the mass density. For our hexagonal lattices, mass density is calculated as $\rho = M/\left(\frac{\sqrt{3}}{2} a^2 h\right)$, where a is the lattice parameter in the xy plane, and h is the layer thickness. The value of h is calculated by the distance between two neighboring carbon bilayers of M_2CO_2 MXene, which is similar to the calculation of graphene[61]. To accurately describe the interlayer interaction of the bilayers, a damped van der Waals (VDW) correction (DFT-D2)[62] is adopted. The flake length, L, which ranges from 1 to 100 μm, approaching the experimental results[31] are considered. The thermal conductivities along the armchair and zigzag directions are both investigated, similar to the previous study conducted for graphene monoxide[63]. The method for thermal conductivity is verified by calculating the thermal conductivity of graphene (4755.6 $Wm^{-1}K^{-1}$ based on a 5 μm flake length at room temperature). The predicted values are consistent very well with the experimental result[4]. The specific heat[64] and thermal expansion coefficient[44,65] are calculated according to existing methods and our previous work.

The carrier mobility is calculated according to Equation (2), considering electron-phonon coupling[2,8,66].

$$\mu = \frac{e\hbar^3 C}{k_B T m_e^* m_d (E_1^i)^2} \quad (2),$$

here $\hbar$ is the reduced Plank's constant, respectively. m_e^* is the carrier effective mass along the transport direction; m_d is determined by $m_d = \sqrt{m_{ex}^* m_{ey}^*}$, where m_{ex}^* and m_{ey}^* are the effective mass along the x- and y-directions, respectively; E_1^i is the deformation potential constant of the valance-band maximum for holes or conduction-band minimum for electrons along the transport direction, calculated by $E_1^i = \Delta V_i / (\Delta a / a_0)$ with ΔV_i as the energy change of the i^{th} energy band under a small lattice variation Δa and a_0 as the lattice constant along the transport direction; C is the elastic modulus along the transport direction, determined by extrapolation based on the relationship of $C(\Delta a/a)^2/2 = (E - E_0)/S_0$, where $(E - E_0)$ is the change of the total energy under a varying lattice constant with a small step size ($\Delta a/a \sim 0.5\%$) and S_0 is the area of the lattice in the xy plane.

References

1. Yu, L. *et al.* Graphene/MoS_2 hybrid technology for large-scale two-dimensional electronics. *Nano Lett.* **14,** 3055–3063 (2014).
2. Qiao, J., Kong, X., Hu, Z.-X., Yang, F. & Ji, W. High-mobility transport anisotropy and linear dichroism in few-layer black phosphorus. *Nat. Commun.* **5,** 4475 (2014).
3. Novoselov, K. S. *et al.* Electric field effect in atomically thin carbon films. *Science* **306,** 666–669 (2004).
4. Balandin, A. A. *et al.* Superior thermal conductivity of single-layer graphene. *Nano Lett.* **8,** 902–907 (2008).
5. Novoselov, K. S. *et al.* Two-dimensional atomic crystals. *PNAS* **102,** 10451–10453 (2005).
6. Li, L. *et al.* Black phosphorus field-effect transistors. *Nat. Nano*. **9,** 372–377 (2014).
7. Fei, R. *et al.* Enhanced thermoelectric efficiency via orthogonal electrical and thermal conductances in phosphorene. *Nano Lett.* **14,** 6393–6399 (2014).

8. Fei, R. & Yang, L. Strain-engineering the anisotropic electrical conductance of few-layer black phosphorus. *Nano Lett.* **14,** 2884–2889 (2014).
9. Mak, K. F., Lee, C., Hone, J., Shan, J. & Heinz, T. F. Atomically thin MoS_2: A new direct-gap semiconductor. *Phys. Rev. Lett.* **105,** 136805 (2010).
10. van der Zande, A. M. *et al.* Grains and grain boundaries in highly crystalline monolayer molybdenum disulphide. *Nat. Mater.* **12,** 554–561 (2013).
11. Xu, M., Liang, T., Shi, M. & Chen, H. Graphene-like two-dimensional materials. *Chem. Rev.* **113,** 3766–3798 (2013).
12. Partoens, B. & Peeters, F. M. From graphene to graphite: Electronic structure around the *K* point. *Phys. Rev. B* **74,** 075404 (2006).
13. Song, L. *et al.* Large scale growth and characterization of atomic hexagonal boron nitride layers. *Nano Lett.* **10,** 3209–3215 (2010).
14. Yan, R. *et al.* Thermal conductivity of monolayer molybdenum disulfide obtained from temperature-dependent raman spectroscopy. *Acs Nano* **8,** 986–993 (2013).
15. Radisavljevic, B., Radenovic, A., Brivio, J., Giacometti, V. & Kis, A. Single-layer MoS_2 transistors. *Nat. Nano* **6,** 147–150 (2011).
16. Wood, J. D. *et al.* Effective passivation of exfoliated black phosphorus transistors against ambient degradation. *Nano Lett.* **14,** 6964–6970 (2014).
17. Naguib, M. *et al.* Two-dimensional nanocrystals produced by exfoliation of Ti_3AlC_2. *Adv. Mater.* **23,** 4248–4253 (2011).
18. Naguib, M. *et al.* Two-dimensional transition metal carbides. *Acs Nano* **6,** 1322–1331 (2012).
19. Naguib, M. *et al.* New two-dimensional niobium and vanadium carbides as promising materials for Li-Ion Batteries. *J. Am. Chem. Soc.* **135,** 15966–15969 (2013).
20. Halim, J. *et al.* Transparent conductive two-dimensional titanium carbide epitaxial thin films. *Chem. Mater.* **26,** 2374–2381 (2014).
21. Naguib, M., Mochalin, V. N., Barsoum, M. W. & Gogotsi, Y. 25th anniversary article: MXenes: a new family of two-dimensional materials. *Adv. Mater.* **26,** 992–1005 (2014).
22. Ghidiu, M. *et al.* Synthesis and characterization of two-dimensional Nb_4C_3 (MXene). *Chem. Commun.* **50,** 9517–9520 (2014).
23. Barsoum, M. W. & Radovic, M. Elastic and mechanical properties of the MAX phases. *Annu. Rev. Mater. Res.* **41,** 195–227 (2011).
24. Zhou, J. *et al.* A two-dimensional zirconium carbide by selective etching of Al_3C_3 from nanolaminated $Zr_3Al_3C_5$. *Angew. Chem. Int. Ed.* **128,** 5092–5097 (2016).
25. Anasori, B. X. Y., Beidaghi, M., Lu, J., Hosler, B. C., Hultman, L., Kent, P. R. C., Gogotsi, Y. & Barsoum, M. W. Two-dimensional, ordered, double transition metals carbides (MXenes). *Acs Nano* **9,** 9507 (2015).
26. Khazaei, M., Arai, M., Sasaki, T., Estili, M. & Sakka, Y. The effect of the interlayer element on the exfoliation of layered Mo_2AC (A = Al, Si, P, Ga, Ge, As or In) MAX phases into two-dimensional Mo_2C nanosheets. *Sci.Technol. Adv. Mater.* **15,** 014208 (2014).
27. Hu, Q. *et al.* Two-dimensional Sc_2C: A reversible and high-capacity hydrogen storage material predicted by first-principles calculations. *Int. J. Hydrogen Energ.* **39,** 10606–10612 (2014).
28. Naguib, M. *et al.* MXene: a promising transition metal carbide anode for lithium-ion batteries. *Electrochem. Commun.* **16,** 61–64 (2012).
29. Tang, Q., Zhou, Z. & Shen, P. Are MXenes promising anode materials for Li ion batteries? Computational studies on electronic properties and Li storage capability of Ti_3C_2 and $Ti_3C_2X_2$(X = F, OH) monolayer. *J. Am. Chem. Soc.* **134,** 16909–16916 (2012).
30. Lukatskaya, M. R. *et al.* Cation intercalation and high volumetric capacitance of two-dimensional titanium carbide. *Science* **341,** 1502–1505 (2013).
31. Ghidiu, M., Lukatskaya, M. R., Zhao, M.-Q., Gogotsi, Y. & Barsoum, M. W. Conductive two-dimensional titanium carbide 'clay' with high volumetric capacitance. *Nature* **516,** 78–81 (2014).
32. Peng, Q. *et al.* Unique lead adsorption behavior of activated hydroxyl group in two-dimensional titanium carbide. *J. Am. Chem. Soc.* **136,** 4113–4116 (2014).
33. Mashtalir, O. *et al.* Intercalation and delamination of layered carbides and carbonitrides. *Nat. Commun.* **4,** 1716 (2013).
34. Gan, L.-Y., Zhao, Y.-J., Huang, D. & Schwingenschlögl, U. First-principles analysis of MoS_2/Ti_2C and MoS_2/Ti_2CY_2 (Y=F and OH) all-2D semiconductor/metal contacts. *Phys. Rev. B* **87,** 245307 (2013).
35. Ma, Z. *et al.* Tunable band structures of heterostructured bilayers with transition-metal dichalcogenide and MXene monolayer. *J. Phys. Chem. C* **118,** 5593–5599 (2014).
36. Zha, X.-H. *et al.* Promising electron mobility and high thermal conductivity in Sc_2CT_2(T = F, OH) MXenes. *Nanoscale* **8,** 6110–6117 (2016).
37. Lai, S. *et al.* Surface group modification and carrier transport properties of layered transition metal carbides (Ti_2CT_x, T: –OH, –F and –O). *Nanoscale* **7,** 19390–19396 (2015).
38. Xie, Y. *et al.* Role of surface structure on Li-ion energy storage capacity of two-dimensional transition-metal carbides. *J. Am. Chem. Soc.* **136,** 6385–6394 (2014).
39. Eames, C. & Islam, M. S. Ion Intercalation into two-dimensional transition-metal carbides: global screening for new high-capacity battery materials. *J. Am. Chem. Soc.* **136,** 16270–16276 (2014).
40. Gan, L.-Y., Huang, D. & Schwingenschlögl, U. Oxygen adsorption and dissociation during the oxidation of monolayer Ti_2C. *J. Mater. Chem. A* **1,** 13672 (2013).
41. Zha, X.-H. *et al.* Role of the surface effect on the structural, electronic and mechanical properties of the carbide MXenes. *EPL (Europhysics Letters)* **111,** 26007 (2015).
42. Khazaei, M. *et al.* Novel electronic and magnetic properties of two-dimensional transition metal carbides and nitrides. *Adv. Funct. Mater.* **23,** 2185–2192 (2013).
43. Heyd, J., Peralta, J. E., Scuseria, G. E. & Martin, R. L. Energy band gaps and lattice parameters evaluated with the Heyd-Scuseria-Ernzerhof screened hybrid functional. *J Chem. Phys.* **123,** 174101 (2005).
44. Mounet, N. & Marzari, N. First-principles determination of the structural, vibrational and thermodynamic properties of diamond, graphite, and derivatives. *Phys. Rev. B* **71,** 205214 (2005).
45. Lide, D. R. ed. *CRC Handbook of chemistry and physics* (84th ed.) CRC Press. Boca Raton, (Florida, 2003).
46. Khazaei, M., Arai, M., Sasaki, T., Estili, M. & Sakka, Y. Two-dimensional molybdenum carbides: potential thermoelectric materials of the MXene family. *Phys. Chem. Chem. Phys.* **16,** 7841 (2014).
47. Synder G. J. & Toberer E. S. Complex thermoelectric materials. *Nat. Mater.* **7,** 105 (2008).
48. Eklund, P., Beckers, M., Jansson, U., Hogberg, H. & Hultman, L. The $M_{n+1}AX_n$ phases: Materials science and thin-film processing. *Thin Solid Films* **518,** 1851–1878 (2010).
49. Kresse, G. & Furthmüller, J. Efficient iterative schemes for *ab initio* total-energy calculations using a plane-wave basis set. *Phys. Rev. B* **54,** 11169–11186 (1996).
50. Perdew, J. P., Burke, K. & Ernzerhof, M. Generalized gradient approximation made simple. *Phys. Rev. Lett.* **77,** 3865–3868 (1996).
51. Heyd, J., Scuseria, G. E. & Ernzerhof, M. Hybrid functionals based on a screened Coulomb potential. *J. Chem. Phys.* **118,** 8207–8215 (2003).
52. Paier, J. *et al.* Screened hybrid density functionals applied to solids. *J. Chem. Phys.* **124,** 154709 (2006).
53. Blöchl, P. E. Projector augmented-wave method. *Phys. Rev. B* **50,** 17953–17979 (1994).
54. Turney, J. E., Landry, E. S., McGaughey, A. J. H. & Amon, C. H. Predicting phonon properties and thermal conductivity from anharmonic lattice dynamics calculations and molecular dynamics simulations. *Phys. Rev. B* **79** (2009).
55. Tang, W., Sanville, E. & Henkelman, G. A grid-based Bader analysis algorithm without lattice bias. *J. Phys.: Condens. Mat.* **21,** 084204 (2009).

56. Momma, K. & Izumi, F. VESTA 3 for three-dimensional visualization of crystal, volumetric and morphology data. *J. Appl. Crystallogr*. **44,** 1272–1276 (2011).
57. Togo, A., Oba, F. & Tanaka, I. First-principles calculations of the ferroelastic transition between rutile-type and $CaCl_2$-type SiO_2 at high pressures. *Phys. Rev. B* **78,** 134106 (2008).
58. Gonze, X. & Lee, C. Dynamical matrices, Born effective charges, dielectric permittivity tensors, and interatomic force constants from density-functional perturbation theory. *Phys. Rev. B* **55,** 10355–10368 (1997).
59. Klemens, P. G. & Pedraza, D. F. Thermal conductivity of graphite in the basal plane. *Carbon* **32,** 735–741 (1994).
60. Klemens, P. G. Theory of thermal conduction in thin ceramic films. *Int. J. Thermophys.* **22,** 265–275 (2001).
61. Andrew, R. C., Mapasha, R. E., Ukpong, A. M. & Chetty, N. Mechanical properties of graphene and boronitrene. *Phys. Rev. B* **85,** 125428 (2012).
62. Grimme, S. Semiempirical GGA-type density functional constructed with a long-range dispersion correction. *J. Comput. Chem.* **27,** 1787–1799 (2006).
63. Pu, H. H. *et al.* Anisotropic thermal conductivity of semiconducting graphene monoxide. *Appl. Phys. Lett.* **102,** 223101 (2013).
64. Upadhyay Kahaly, M. & Waghmare, U. V. Size dependence of thermal properties of armchair carbon nanotubes: A first-principles study. *Appl. Phys. Lett.* **91,** 023112 (2007).
65. Zha, X.-H., Zhang, R.-Q. & Lin, Z. Point defect weakened thermal contraction in monolayer graphene. *J Chem. Phys.* **141,** 064705 (2014).
66. Bruzzone, S. & Fiori, G. Ab-initio simulations of deformation potentials and electron mobility in chemically modified graphene and two-dimensional hexagonal boron-nitride. *Appl. Phys. Lett.* **99,** 222108 (2011).

Acknowledgements

The authors acknowledge the support of the Division of Functional Materials and Nanodevices, Ningbo Institute of Materials Technology and Engineering, Chinese Academy of Sciences, the National Natural Science Foundation of China (Grant Nos 51372046, 51479037 and 91226202), the Ningbo Municipal Natural Science Foundation (Nos 2014A61006 and 2016A610272), ITaP at Purdue University for computing resources and the key technology of nuclear energy, 2014, CAS Interdisciplinary Innovation Team.

Author Contributions

X.-H.Z., S.D. and Q.H. designed the research. X.-H.Z. and S.D. conducted the theoretical calculation and wrote the paper. J.H., H.H., J.Z. and J.S.F. contributed to the scientific discussion.

Additional Information

Supplementary information accompanies this paper at http://www.nature.com/srep

Competing financial interests: The authors declare no competing financial interests.

How to cite this article: Zha, X.-H. *et al.* The thermal and electrical properties of the promising semiconductor MXene Hf_2CO_2. *Sci. Rep.* **6**, 27971; doi: 10.1038/srep27971 (2016).